

<b>REPORT DOCUMENTATION PAGE</b>					<i>Form Approved OMB No. 0704-0188</i>	
<small>The public reporting burden for this collection of information is estimated to average 1 hour per response, including the time for reviewing instructions, searching existing data sources, gathering and maintaining the data needed, and completing and reviewing the collection of information. Send comments regarding this burden estimate or any other aspect of this collection of information, including suggestions for reducing the burden, to Department of Defense, Washington Headquarters Services, Directorate for Information Operations and Reports (0704-0188), 1215 Jefferson Davis Highway, Suite 1204, Arlington, VA 22202-4302. Respondents should be aware that notwithstanding any other provision of law, no person shall be subject to any penalty for failing to comply with a collection of information if it does not display a currently valid OMB control number.</small>						
<b>PLEASE DO NOT RETURN YOUR FORM TO THE ABOVE ADDRESS.</b>						
<b>1. REPORT DATE (DD-MM-YYYY)</b>		<b>2. REPORT TYPE</b>			<b>3. DATES COVERED (From - To)</b>	
<b>4. TITLE AND SUBTITLE</b>				<b>5a. CONTRACT NUMBER</b>		
				<b>5b. GRANT NUMBER</b>		
				<b>5c. PROGRAM ELEMENT NUMBER</b>		
<b>6. AUTHOR(S)</b>				<b>5d. PROJECT NUMBER</b>		
				<b>5e. TASK NUMBER</b>		
				<b>5f. WORK UNIT NUMBER</b>		
<b>7. PERFORMING ORGANIZATION NAME(S) AND ADDRESS(ES)</b>					<b>8. PERFORMING ORGANIZATION REPORT NUMBER</b>	
<b>9. SPONSORING/MONITORING AGENCY NAME(S) AND ADDRESS(ES)</b>					<b>10. SPONSOR/MONITOR'S ACRONYM(S)</b>	
					<b>11. SPONSOR/MONITOR'S REPORT NUMBER(S)</b>	
<b>12. DISTRIBUTION/AVAILABILITY STATEMENT</b>						
<b>13. SUPPLEMENTARY NOTES</b>						
<b>14. ABSTRACT</b>						
<b>15. SUBJECT TERMS</b>						
<b>16. SECURITY CLASSIFICATION OF:</b>			<b>17. LIMITATION OF ABSTRACT</b>	<b>18. NUMBER OF PAGES</b>	<b>19a. NAME OF RESPONSIBLE PERSON</b>	
a. REPORT	b. ABSTRACT	c. THIS PAGE			<b>19b. TELEPHONE NUMBER (Include area code)</b>	

## FINAL REPORT

# **MULTI-STATIC DETECTION AND LOCALIZATION OF BURIED TARGETS USING SYNTHETIC APERTURE ITERATIVE TIME-REVERSAL PROCESSING**

H. C. Song, Karim Sabra, W. A. Kuperman, and W. S. Hodgkiss  
Marine Physical Laboratory of the Scripps Institution of Oceanography  
University of California, San Diego  
La Jolla, CA 92093-0238

Phone: (858) 534-0954 Fax: (858) 534-7641 E-mail: [hcsong@ucsd.edu](mailto:hcsong@ucsd.edu)  
Phone: (858) 822-3155 Fax: (858) 534-7641 E-mail: [ksabra@ucsd.edu](mailto:ksabra@ucsd.edu)  
Phone: (858) 534-7990 Fax: (858) 534-8801 E-mail: [wkuperman@ucsd.edu](mailto:wkuperman@ucsd.edu)  
Phone: (858) 534-1798 Fax: (858) 534-1798 E-mail: [whodgkiss@ucsd.edu](mailto:whodgkiss@ucsd.edu)

## **LONG-TERM GOAL**

To use an iterative time-reversal technique to provide robust focusing along the ocean bottom, with little signal processing effort involved and a-priori information on the environment, to enhance the detection and localization of a proud or buried target in shallow water.

## **OBJECTIVES**

The objective of the proposed MPL component of a SWAMSI continuation will develop bi-static applications of the iterative time reversal techniques to focus along the ocean bottom. Iterative time-reversal provides a simple solution for self-adaptive focusing on strong reflectors (i.e. scattering targets) located on the ocean bottom without relying on predictive or modeling capabilities of the environment and of the target of interest. These robust focusing properties are crucial for mapping large and uncharted areas with little signal processing effort involved. With the experiments planned by Schmidt et al, there will be enough data to understand the ultimate limitations of the proposed self adaptive methods.

## **BACKGROUND FOR FOCUSING CONCEPT**

The robust focusing and pulse compression provided by time reversal techniques can be exploited to enhance active sonar processing in shallow water environments. A successful time-reversing array (TRA) retrofocus can be created without any prior knowledge of the environment, the probe source or the reflector location, or the array's transducer locations. A TRA may be of nearly any size or shape and may operate in any frequency range. Moreover, TRAs with sufficient aperture perform well in multipath environments.

# FINAL REPORT

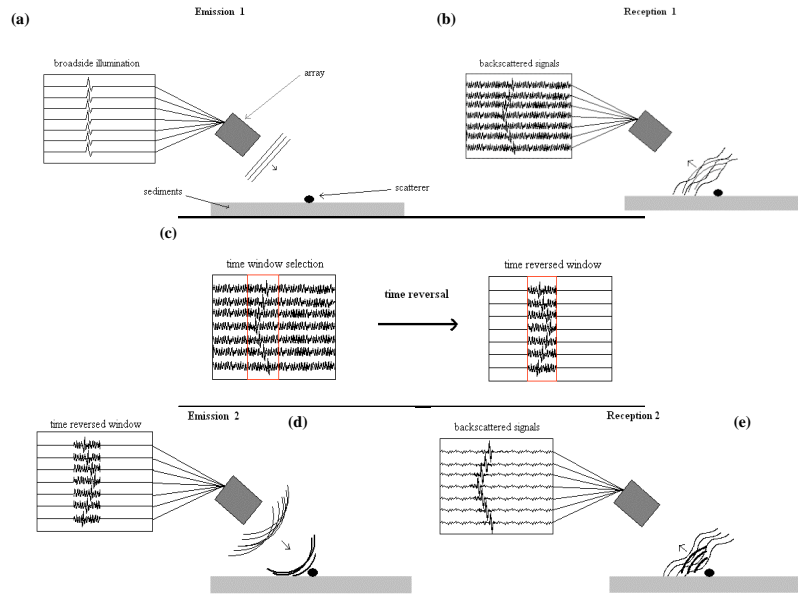


**Figure 1:** Diagram of an Iterative Time-Reversal process in a classical monostatic configuration. 1 iteration is used to enhance focusing on a reflector located above sediments. (a) Broadside illumination with a pulse signal. (b) Backscattered signals are recorded. (c) A time window containing the potential target signal is selected in order to be time-reversed. (d) The resulting wave illuminates the bottom. (e) The backscattered signals reveal that the waves focused on the target since the target echo is enhanced. Further iterations can help detect weaker targets.

Thus the (iterative) time reversal process can provide a means for self-adaptive focusing in the vicinity of the water-bottom interface in order to improve the detection of targets laying on the seafloor or buried in the sediments (see Figure 1). By applying this time-reversal process iteratively, we construct a set of signals for the TRA which focus on the strongest scatterer located in the selected range interval. This is achieved by repeating the iterative time-reversal process over a sliding time-gated window portion of the initial reverberation signals recorded in a waveguide, thus allowing us to scan the bottom surface. Reflectivity maps, similar to a sonar map, but with an enhanced contrast for the strongest reflectors (or scatterers), at the water-bottom interface can be constructed using a simple TRA. When the reflectivity contrast between the buried target and the bottom reverberation is sufficient, focusing energy on the target is accomplished with very little signal processing effort. Otherwise, an eigenvector/eigenvalue analysis of the backscattered signals can be applied to isolate the target contribution and to construct appropriate time-reversed signals that focus on the target solely. Hence the iterative time-reversal process should provide a simple solution for separating the echoes of the targets from the reverberation of the ocean bottom.

## FINAL REPORT

In support of our potential iterative and ultimately bi-static concept, we mention the previous passive iterative time reversal implementation. Only the knowledge of the inter-element impulse response matrix for TRA is required, i.e. measuring the backscattered Green's functions (or impulse response) between all pairs of elements of the TRA after round-trip propagation between the TRA elements and the ocean bottom, thus including the whole bottom reverberation response. The acquisition of the inter-element impulse response matrix is the only active part of the processing. The full physical propagation characteristics between the TRA and the ocean floor are then contained in the inter-element impulse responses at once, and no extra information is required. The various steps of the time-reversal process, as described in Fig. 1 can then be implemented passively by simply performing correlations of these inter-element signals with the time-gated window of the reverberation signals selected at the previous iterations. This allows us to construct passively the reverberation time-series of each TRA element as if successive back and forth propagation between the TRA and the ocean floor had occurred. Then, the time reversal iterations can be implemented passively.

This passive iterative time-reversal technique was applied to detect a target (composed of 8 small glass spheres) with a curtain source receive array (SRA) used as a time-reversal array (having a small vertical aperture of 8 by 1.5m, operating from 3 to 4 kHz) that is a surrogate for existing sonar systems in a mono-static configuration (see Fig 1). The curtain SRA was deployed in 50m shallow water and the target was located approximately on the bottom 203m away from the SRA, and the inter-element response was measured over 3min. This reverberation focusing technique appears robust with respect to environmental fluctuations. A reflectivity map was constructed for one iteration of the time-reversal process (see Figure 2.a and 2.b). The target appears at the estimated range as a bright spot in the main diagonal delimited by the extent of time-gated window used to construct time-reversed reverberation signals (see Figure 1). Detection of the target is enhanced over a conventional broadside return (see Figure 2.c).

## PROPOSED RESEARCH ITEMS

- 1) Develop and validate synthetic, iterative *time reversal aperture* for SWAMSI
- 2) Relate and understand the performance of the above procedure to the near field measurements that are being performed simultaneously
- 3) Extend the processing method to a cooperating multi-platform scenario

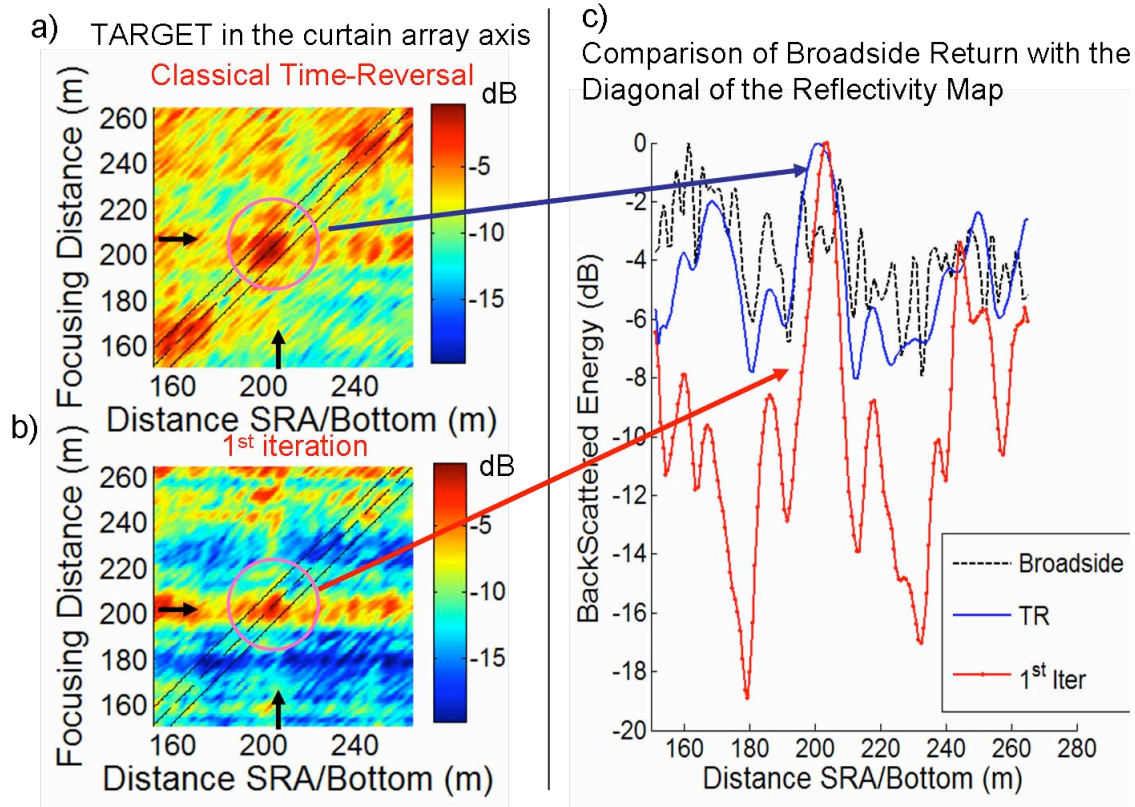


**Figure 2:** a) and b) Reflectivity maps for a target, located 203m away from the SRA. These maps were computed over sliding time-gated hanning window portion of  $\Delta=20ms$  of the reverberation signals (delimited by the dashed lines along the main diagonal) for: a) the time-reversal process or b) 1 iteration, of the time-reversal process. The horizontal axis is the recording time (i.e. the round trip propagation) converted to the SRA/bottom distance,  $d=t c_0/2$  ( $c_0=1515m/s$ ) between the SRA to the bottom. The vertical axis is the average intended focusing distance along the bottom being scanned by the TRA corresponding to the selected time-gated window. Note the contrast improvement achieved for the strongest reflectors by using one iteration. The target location is the brightest spot at 203m. c) Comparison of the initial broadside return to the diagonal of the reflective map after iterative time-reversal.

## APPROACH

### NURC MCM'06 Experiment: Application to bi-static detection enhancement.

Our method requires the addition of a moving (suspended, drifting) receiver that has a common sync to the TOPAS source. The previous Passive Iterative Time Reversal technique can be applied to a dynamic bi-static geometry where the source and receiver roles are separate. The active source is provided by a TOPAS parametric source, mounted on a telescopic tower, insonifying a target, as per Schmidt et al. At the same time, a moving receiver (e.g. towed hydrophone from a surface platform) collects the bi-static

## FINAL REPORT

backscatter signals from the target at several positions along its trajectory. These data are then used to construct a synthetic aperture Time-Reversal Array which can be used for the passive iterative time-reversal process.

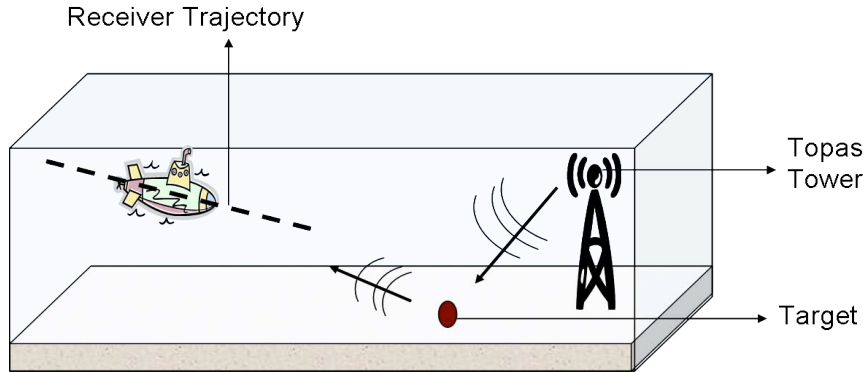


**Figure 3:** Schematic of bi-static implementation of time-reversal process for detection and localization of Target in shallow water. The Topas tower provides successive illumination of the target. A moving receiver (e.g. towed hydrophone from a surface platform, AUV...) collects the bi-static backscatter signals from the target at several positions along its trajectory. This moving receiver can then be used to construct a synthetic aperture Time-Reversal Array which can be used for the passive iterative time-reversal process.

Only a rough estimate of the trajectory is necessary to estimate the relative position of the synthetic aperture TRA elements with respect to the target location. This allows one to estimate which bottom patch corresponds to a specific given time-gated window of the backscatter signals in order to perform a search for the target along the seafloor (see Fig. 4). Reflectivity Maps (similar to Fig. 2) over the whole search grid could then be generated to help detect and localize the target.

Validation of the detection capabilities of the synthetic aperture time-reversal processing in this simple bi-static geometry would provide an initial demonstration for self-adaptive and robust MCM application eventually involving AUVs. The data/analysis done in the near field by Schmidt et al will also be studied in the context of relating the decomposition of the TR process to the complex elastic-properties of the combination of target-sediment.

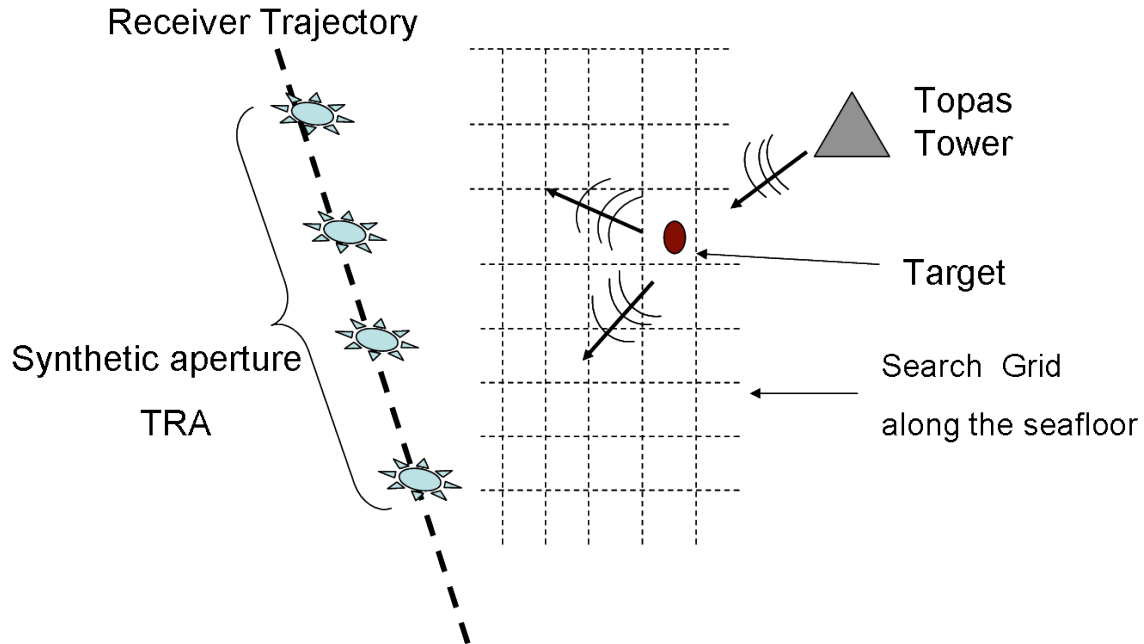


**Figure 4:** Top view implementation for the Target using a synthetic aperture Time-Reversal Array. Search grid along the the seafloor can be constructed using an estimated position of the Synthetic aperture TRA with respect to the ocean bottom, based on simple navigation data. Reflectivity map similar to Fig. 2 can then be constructed over the whole search grid.

### SWAMSI-2nd Experiment

Although beyond the time frame of this proposal, it is likely that a second SWAMSI experiment will be conducted in FY08. The algorithms developed here will be available for use in the FY08 experiment which will involve multiple platforms.

**Personnel:** In addition to the PI's, there will be some programming/data work provided by the appropriate MPL staff.

**Results:** The results of this project have led to new algorithms for SWAMSI experiments and are summerarized in the follow extract from W. Higley's thesis:

## **Chapter 5**

### **Detection of Resonances on a Spherical Target**

#### abstract

The use of low frequency (2-15 kHz) acoustic signals for mine countermeasures have been motivated by the chance to use scattering features of buried targets (e.g. the radius, wave thickness, and elastic properties) in the classification of the target. At frequencies, lower than traditionally used, sound penetrates into the sediment better and excites less signal-generated noise off the seabed. The structural waves of typical mine-sized targets are enhanced at these frequencies. This paper introduces and compares two forms of processing designed to classify a target as resonant or non-resonant based on the backscattered field. The two forms of processing are distinguished as an incoherent, energy-based method, and a coherent method based on the concept of principal component analysis (PCA).

#### **5.1 Introduction**

When performing mine countermeasures (MCM), it is preferable to have a large standoff distance. That is, it is desirable to detect and classify a mine while as far away as possible from it. This desire leads to the use of lower frequencies, which propagate further horizontally. This decreases the resolution of traditional acoustic imaging techniques. Also, the increase in standoff distance leads to an increase in the influence of the waveguide in introducing multipath.



Recent experiments [1],[2] have attempted to use low frequency (2-15 kHz) signals as part of the target detection and classification problem of MCM. At this low frequency, although the resolution of traditional imaging is limited, other properties such as the radius, wall thickness, and elastic properties of the target can be extracted.

Lower frequencies also benefit from greater seabed penetration. Attenuation above the grazing angle decreases approximately linearly with frequency, and below the grazing angle the evanescent lateral wave field in the bottom penetrates deeper [3]. The signal-generated noise from reverberation off surface features of the seafloor (such as sand ripples) will also decrease with frequency [4].

The problem of using target resonances to classify a target is complicated in a waveguide by the multipath in the environment. This paper compares two forms of processing on two targets in both freespace and in a waveguide. The two forms of processing are classified as an incoherent, energy-based processing method, and a coherent method based on the concept of principal component analysis (PCA). Our simulations show the benefit of the coherent method over the incoherent method in classifying a target as resonant or non-resonant. Finally, this paper proposes an experiment using a horizontally-aligned array towed from an autonomous underwater vehicle (AUV).

## 5.2 Freespace Simulation

A freespace simulation is done to test the feasibility of our processing. In an aqueous medium with a density of  $1 \text{ g/cm}^3$  and a sound speed of  $1507 \text{ m/s}$ , there is an array of nine hydrophones arranged vertically with a separation distance of  $10 \text{ m}$ . The target is

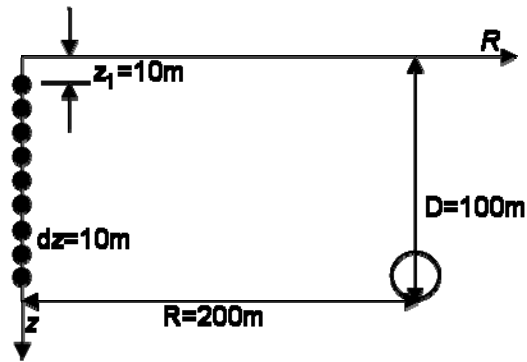


Figure 5.1: The geometry of the simulation. A vertical array consisting of nine elements is oriented vertically in freespace. The distance between each element is 10 m, and the first element is considered 10 m below some arbitrary origin. The target is located such that the bottom of the target is 10 m below the lowest element, and 200 m away from the vertical array.

situated such that the bottom is located 10 m below the lowest source/receiver, and the center is located 200 m away horizontally. The geometry of the set-up is shown in Fig. 5.1. Two targets are analyzed: a bubble and a spherical shell. The bubble is a spherical vacuum with a radius of .53 m. The spherical shell has an inner radius of .5 m and an outer radius of .53 m. The interior of the shell is a vacuum, and the shell itself is composed of steel with a density of  $7.7 \text{ g/cm}^3$ , a shear sound speed of 2940 m/s and a compressional sound speed of 5880 m/s. The two targets are shown in Fig. 5.2.

Each hydrophone transmits and pulse which is back-scattered by the target and received on all nine hydrophones. This creates a three-dimensional matrix for each target as a function of transmitter depth, source depth, and frequency. The matrices for the bubble and the sphere are denoted as  $\mathbf{K}_b(z_t, z_s, \omega)$  and  $\mathbf{K}_s(z_t, z_s, \omega)$ , respectively. By taking the inverse Fourier transform along the frequency domain, one can examine the received field for any given transmitter. In Fig. 5.3, the freespace responses from the first transmitter for both the bubble and the shell are shown. The response from the bubble is

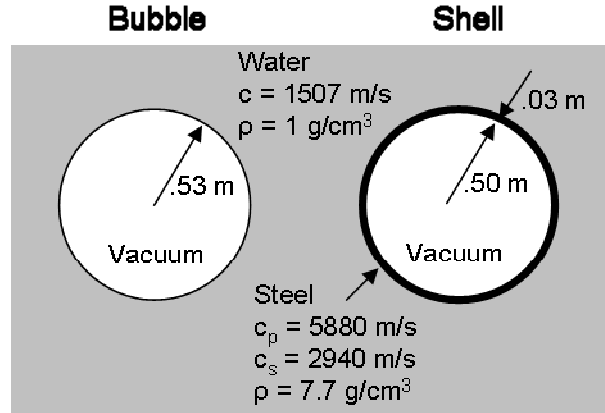


Figure 5.2: The two targets, both located in an aqueous medium. The first target is a bubble, whose interior is a vacuum. The radius of .53 m is matched to the outer radius of the second target, a resonant shell. The wall thickness of the shell is 3 cm, and it is also filled with a vacuum. The speed of sound and density of the water are 1507 m/s and 1 g/cm<sup>3</sup> respectively. The shell is composed of steel with a density of 7.7 g/cm<sup>3</sup>. The sound speeds of compression and shear waves in the steel are 5880 m/s and 2940 m/s respectively.

composed of only a specular component, that field that reflects off the surface of the bubble. However, the response from the shell is composed of the same specular component (possibly phase-shifted) and an additional resonant component that arrives later.

Given the matrices  $\mathbf{K}_b(z_t, z_s, \omega)$  and  $\mathbf{K}_s(z_t, z_s, \omega)$ , it is desirable to find some processing that will distinguish between the two. As can be seen in Fig. 5.3, in the freespace case, one could simply time-gate out the specular and be left with the resonance, if it existed. However, this method will not work in a waveguide, as will be seen later, so other processing methods need be examined.

The first method considered is an incoherent, energy-based method. The matrix  $\mathbf{K}$  can be reduced to a one-dimensional vector by summing incoherently across transmitters

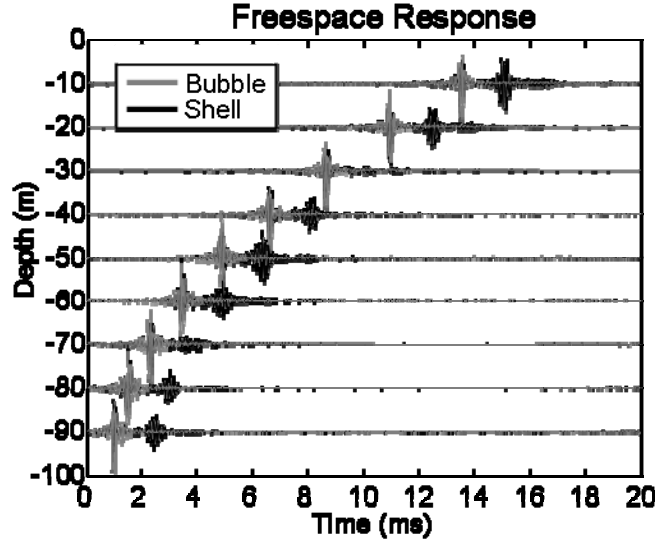


Figure 5.3: The backscattered response on the vertical array from both the bubble (gray) and the shell (black) when excited by a single source on the array. The response from the bubble consists of a strong, single, specular echo, while the response from the shell is composed of both that same specular response, and a resonant component that arrives later.

and receivers. The processing can be expressed mathematically, where  $N$  is the number of hydrophones, as

$$\mathbf{e}(\omega) = \sum_{z_r=1}^N \sum_{z_t=1}^N |\mathbf{K}(z_t, z_r, \omega)|^2. \quad (5.1)$$

This term can also be expressed in terms of the singular value decomposition (SVD) [5]. Each frequency of  $\mathbf{K}$  represents an  $N \times N$  matrix. Taking the singular value decomposition of this matrix yields  $N$  singular values. Thus, there are  $N$  singular values at each frequency. The sum of these singular values squared also yields the vector  $\mathbf{e}(\omega)$ . This is shown mathematically below as [6]:

$$\begin{aligned} \text{svd}(\mathbf{K}(z_t, z_r, \omega)) &\Rightarrow \sigma_i(\omega) \text{ for } i=1, 2, \dots, N \\ \sum_{i=1}^N \sigma_i^2(\omega) &= \sum_{z_r=1}^N \sum_{z_t=1}^N |\mathbf{K}(z_t, z_r, \omega)|^2 = \mathbf{e}(\omega). \end{aligned} \quad (5.2)$$

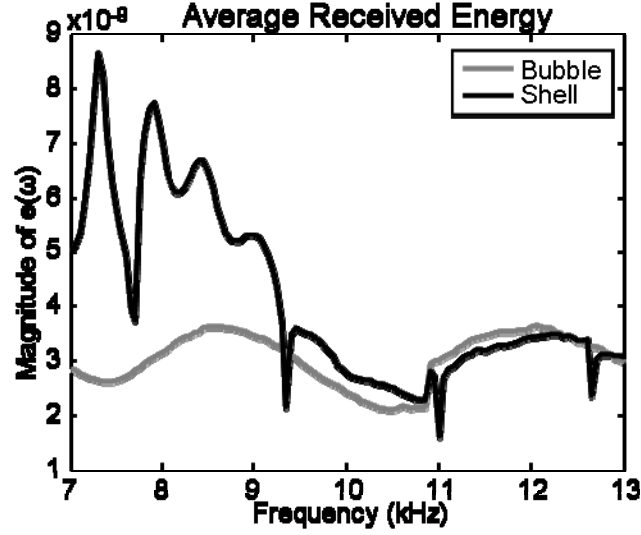


Figure 5.4: The received energy across frequency of the backscattered response of the bubble (gray) and the shell (black), averaged across source and receiver. A few of the resonant peaks of the shell are seen at lower frequencies.

Shown in Fig. 5.4 are the results of this energy-based processing. The resonances of the shell are seen as peaks in the average energy at specific frequencies. The bubble shows no such peaks in the frequency domain, and is rather flat across frequency, as one would expect from a specular echo.

The second method considered is a coherent one related to principal component analysis. We reduce the three-dimensional matrix  $\mathbf{K}(z_t, z_r, \omega)$  into a two-dimensional matrix, labeled  $\hat{\mathbf{K}}(z_t, z_r \cdot \omega)$ , via concatenation. The received field in the frequency domain from each source can be thought of as a separate observation of a random vector. From these observations, a sample covariance matrix can be created as follows:

$$\mathbf{S}(z_r \cdot \omega) = \frac{1}{N-1} \sum_{z_t=1}^N \hat{\mathbf{K}}(z_t, z_r \cdot \omega) \hat{\mathbf{K}}^H(z_t, z_r \cdot \omega). \quad (\text{S.3})$$

Taking the first eigenvector of the matrix  $\mathbf{S}$  yields the first principal component of the data [6]. The first principal component is the energy-constrained vector which maximizes the average correlation with the data. It can be thought of as the part of the data that is the most similar across all observations, or in the case examined here, across all sources. We write the first principal component mathematically as:

$$\mathbf{p}(z_r \cdot \omega) = \arg \max_{\mathbf{p}} \sum_{z_t=1}^N \left| \mathbf{p}^H(z_r \cdot \omega) \hat{\mathbf{K}}(z_t, z_r \cdot \omega) \right|^2. \quad (\text{S.4})$$

As stated above,  $\mathbf{p}$  is also the first eigenvector of the sample covariance matrix,  $\mathbf{S}$ . The vector  $\mathbf{p}$  can be found another way, using singular value decomposition. If we consider  $\mathbf{S}$  to have the following eigenvalue decomposition,

$$\mathbf{S} = \mathbf{U} \mathbf{\Lambda} \mathbf{U}^H, \quad (\text{S.5})$$

we can write the singular value decomposition of  $\hat{\mathbf{K}}$  as

$$\hat{\mathbf{K}} = \mathbf{U} \sqrt{(N-1)\mathbf{\Lambda}} \mathbf{V}^H. \quad (\text{S.6})$$

In both cases, the matrix  $\mathbf{U}$  is identical. The principal component,  $\mathbf{p}$ , can be thought of as either the first eigenvector of  $\mathbf{S}$ , or the first left singular vector of  $\hat{\mathbf{K}}$ .

Deconcatenation of the vector  $\mathbf{p}(z_r \cdot \omega)$  results in a matrix  $\mathbf{P}(z_r, \omega)$  that is a function of receiver and frequency. Taking the inverse Fourier transform along the frequency domain yields a single time-domain field for each matrix,  $\mathbf{K}_b$  and  $\mathbf{K}_s$ . These fields are plotted in Fig. 5.5. The fields shown below can be thought of as the parts of the received fields that are most independent of source depth. In the case of the bubble, there is a strong first arrival as there is similarity between the specular echoes for each source. In the case of the shell, the resonance is nearly separated from the specular, as the resonance

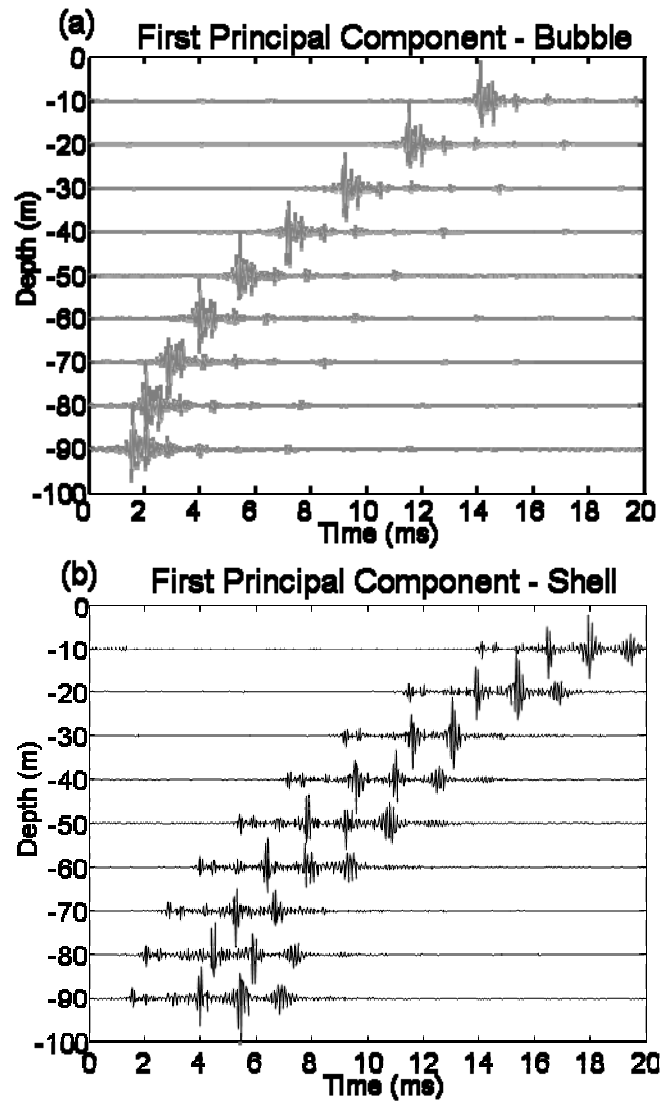


Figure 5.5: The first principal component from the bubble (gray) and the shell (black). The coherent processing first yields a field, which is shown in these figures. The field extracted from the bubble is composed of a strong first arrival and weaker later arrivals which may be attributed to weak resonances of the bubble. On the other hand, the extracted field from the shell's response is composed of periodic pulses corresponding to the resonances propagating around the shell.

is entirely source independent. The resonant component of the received field is independent of excitation, and shows up prominently in this processing.

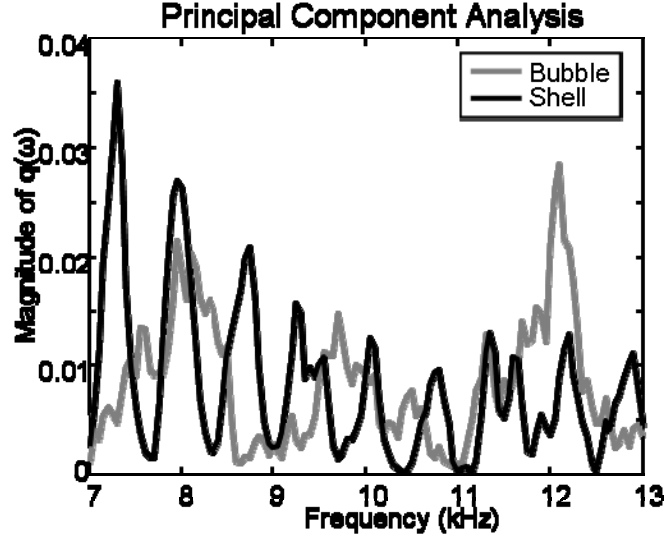


Figure 5.6: The result of the coherent processing on the bubble (gray) and the shell (black). The periodic resonance peaks of the shell are quite pronounced through the frequency range, whereas the response of the bubble is relatively flat, as one would expect for a specular component.

We can reduce the matrix  $\mathbf{P}(z_r, \omega)$  into a frequency vector by summing incoherent across receiver. We can compare this new vector,  $\mathbf{q}(\omega)$ , with the previously calculated incoherent vector,  $\mathbf{e}(\omega)$ . The new vector is written mathematically as:

$$\mathbf{q}(\omega) = \sum_{z_r=1}^N |\mathbf{P}(z_r, \omega)|^2. \quad (\text{S.7})$$

The vector  $\mathbf{q}(\omega)$  is calculated for both the bubble and the sphere, with the results shown in Fig. 5.6. The processing requires the results for both the bubble and the sphere to have the same magnitude, when summed across frequency, as the matrix  $\mathbf{U}$  is unitary, regardless of the relative energy in the matrix  $\mathbf{K}$ . The result of the principal component analysis processing done on the bubble is relatively flat, compared to the results obtained when done on the shell. The resonances of the shell appear again as peaks in the frequency domain, with a spacing of approximately 675 Hz. This corresponds to a



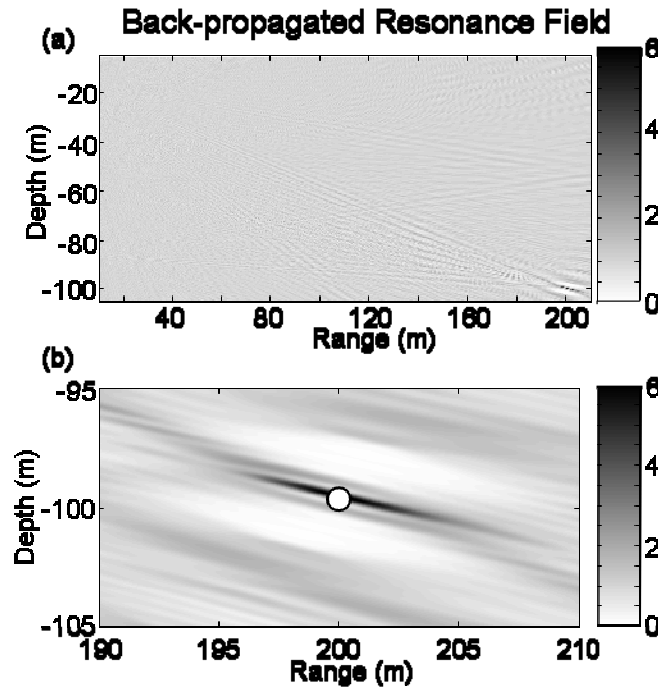


Figure 5.7: The result of back-propagating the field extracted in Fig 5.5b. The focus is seen only at the location of the target, at a depth of 100 m and a range of 200 m.

repeated time-delay of about 1.5 ms, a spacing that is seen in Fig 5b. This is the time it takes the resonance to travel around the sphere before emitting again. From this, we can calculate the group speed of the  $A_0$  wave as approximately 2120 m/s.

Comparing Fig. 5.4 and Fig. 5.6, we notice that the principal component analysis is able to distinguish resonant peaks at 10 kHz and above, whereas the energy-based analysis cannot. Also, those peaks at frequencies less than 10 kHz are more pronounced than in the energy-based analysis.

Returning our attention to the time-domain resonance field of Fig. 5.5b, expressed by the matrix  $\mathbf{P}_s(z_r, \omega)$ , an incoherent back-propagation of this field can be calculated. The result of this calculation is shown in Fig. 5.7. We see that the back-propagated resonance field focuses at a location just above the sphere. The relative tightness of the focus is

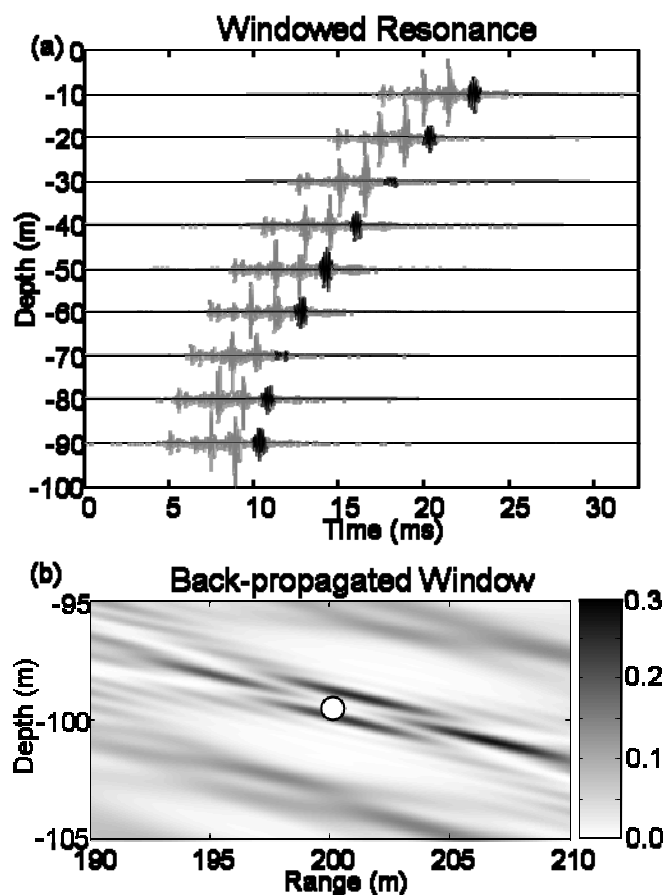


Figure 5.8: a) In gray is the field previously extracted from the shell and shown in Fig. 5.5b. The windowed portion, shown in black, corresponds to a resonant emission from the target. b) The result of back-propagating the resonant emission shows a pair of foci both above and below the location of the target, corresponding to the two locations on the target from which resonances are emitted. The other two foci, in front of and behind the target, are assumed sidelobes, artifacts of the processing.

related to the vertical aperture of the hydrophone array used. Back-propagation of the matrix  $\mathbf{P}_b(z_r, \omega)$  results in a similar focus near the location of the sphere. A difference between the two back-propagated fields can be found by windowing out a single resonance of the matrix  $\mathbf{P}_s(z_r, \omega)$  in the time domain (as shown in Fig. 5.8a) and back-propagating only that piece. As seen in Fig. 5.8b, this results in a group of foci in the area around the sphere. The two middle foci are interpreted at the two patches on the

sphere from which resonances are emitted to the array. The other two, in front and behind the sphere, are interpreted as sidelobes, artifacts of the processing.

### 1.3 Waveguide Simulation

Having established two forms of processing, an incoherent energy-based method yielding  $\mathbf{e}(\omega)$ , and a coherent method based on principal component analysis which yields  $\mathbf{q}(\omega)$ , the case of a buried sphere in a waveguide is now examined. The array is situated vertically as before, in a 100-m deep underwater waveguide. The target is situated 200 m away horizontally, as before, but instead of the bottom of the target being at a depth of 100 m, the top is located at that same position. The target is therefore buried, such that the top of the target is tangent to the waveguide bottom. The noise-free matrices  $\mathbf{K}_b(z_t, z_s, \omega)$  and  $\mathbf{K}_s(z_t, z_s, \omega)$  are acquired as before, and an additional matrix  $\mathbf{K}_r(z_t, z_s, \omega)$  is calculated from a seafloor reverb model, to allow us to examine our processing in the presence of signal-generated noise. The backscattered response of the flush-buried sphere in a waveguide is shown in Fig. 5.9 for the two targets: the bubble and the sphere. The shape of the back-scattered response is the same, but each pulse of the bubble's response is convolved with the resonance in the case of a shell.

The two above-mentioned method of processing are applied now to the case of a flush-buried target. For comparison purposes, each of the vectors  $\mathbf{e}(\omega)$  and  $\mathbf{q}(\omega)$  are normalized such that the energy in each vector is one, which we denote  $\hat{\mathbf{e}}(\omega)$  and  $\hat{\mathbf{q}}(\omega)$ . Figure 5.10 shows the result of both forms of processing, without noise, on both flush-buried targets. In the case of the bubble (Fig. 5.10a), there are no noticeable peaks found in either form of processing, as we would expect from specular echoes. Both the

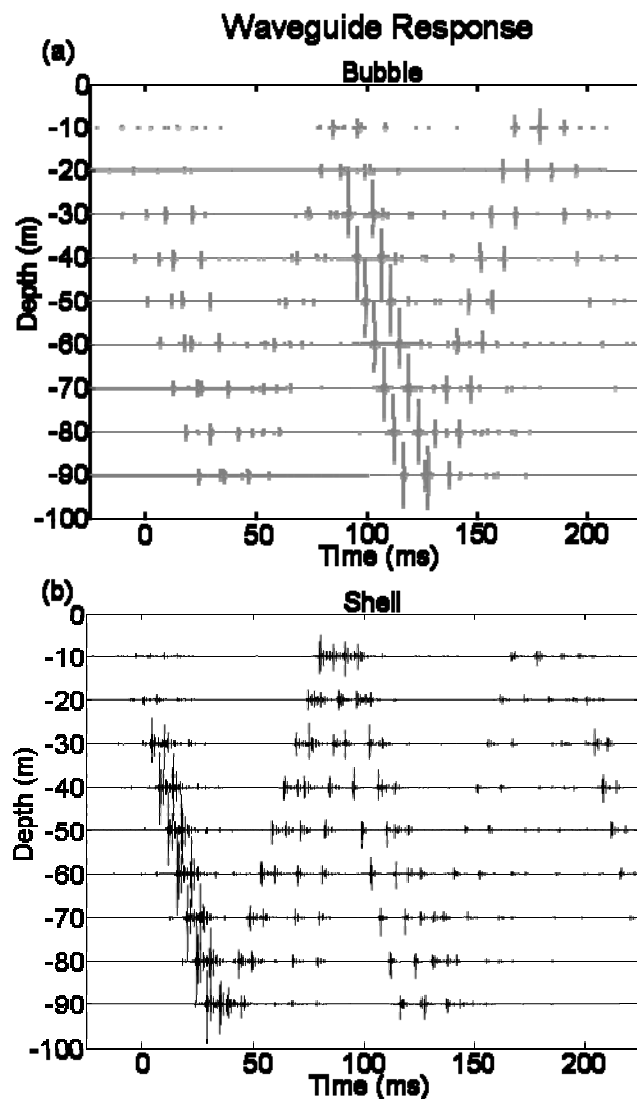


Figure 5.9: The back-scattered response from a flush-buried bubble (gray) or shell (black) in a waveguide. The shape of the response in the same in both cases, but each pulse of the response in the case of the bubble is turned into a resonant arrival structure in the case of the shell.

incoherent and coherent forms of processing yield resonant peaks when applied to the flush-buried shell (Fig. 5.10b), but the method based on principal component analysis causes these peaks to be more pronounced.

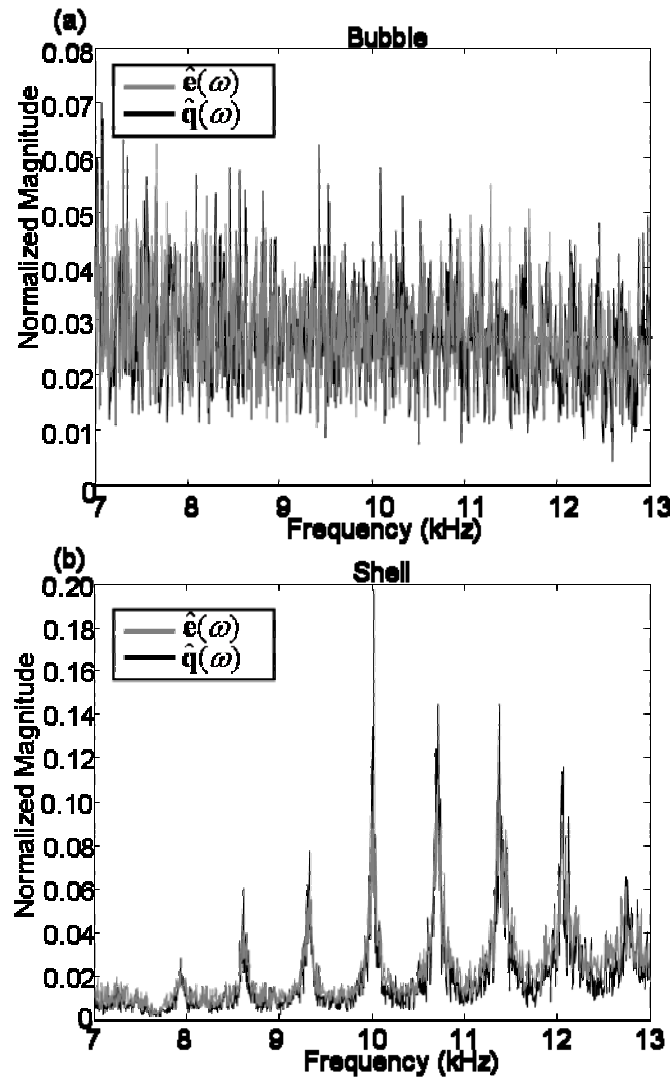


Figure 5.10: a) The result of the incoherent (gray) and coherent (black) processing on the non-resonant bubble in a waveguide. The frequency response is relatively flat, as we would expect from a purely specular echo. b) The result of the incoherent (gray) and coherent (black) processing on the resonant shell in a waveguide. The periodic resonant peaks are clearly identified, and correspond well to those found in freespace (Fig. 5.6).

By examining the results of the processing under various levels of signal-generated noise, a difference is again seen in the results of the incoherent and coherent processing. Figure 5.11 shows the results of both forms of processing on the flush-buried shell for four different noise levels. In Fig. 5.11a, the results are very similar to Fig. 10, with both

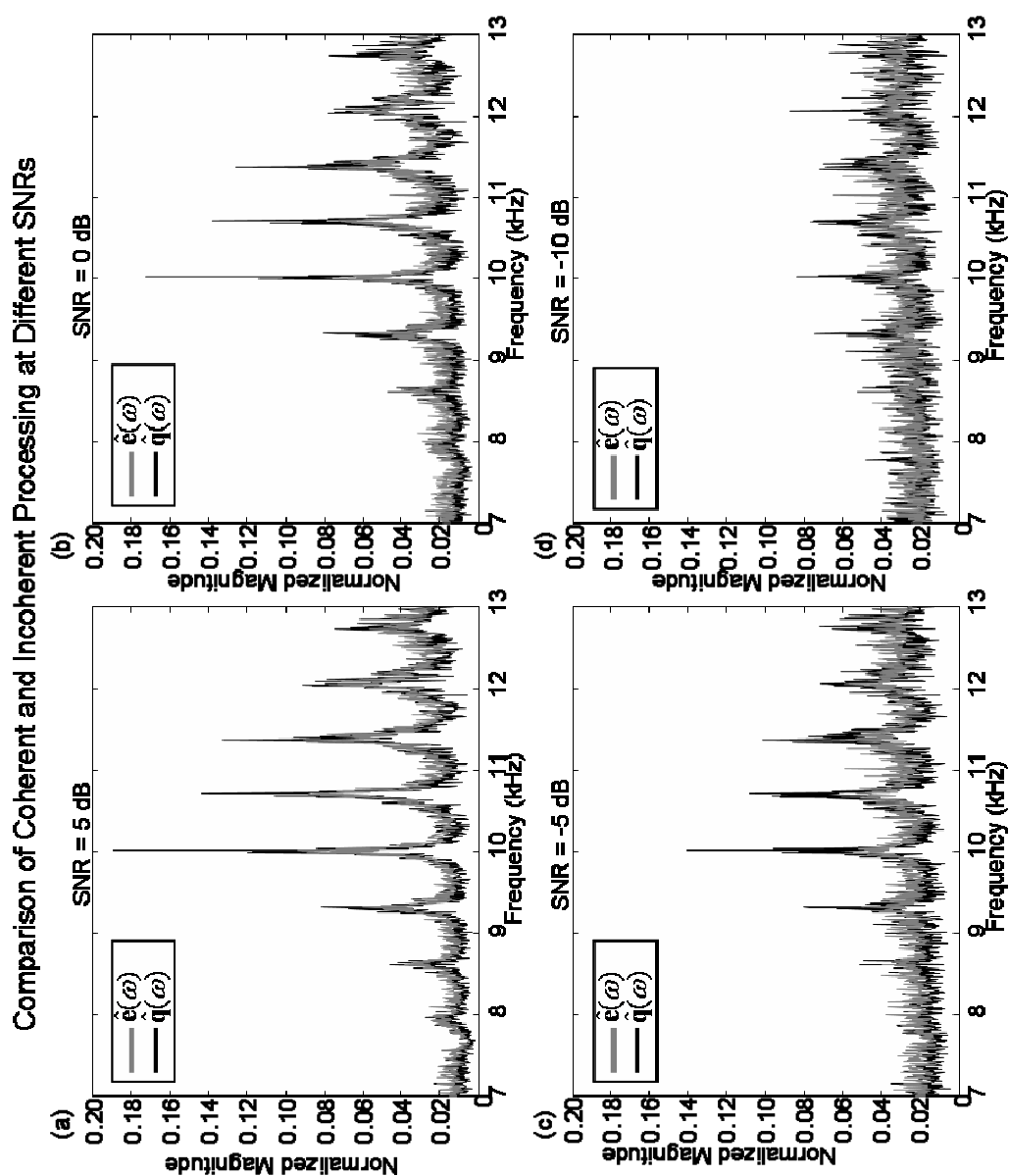


Figure 5.11: A comparison of the incoherent (gray) and coherent (black) processing on the flush-buried shell for four different signal-to-noise ratios. Although both methods degrade as noise increases, the coherent method still shows peaks at -10 dB, whereas the incoherent method fails at this SNR.

forms of processing showing strong resonant peaks, and those of the coherent PCA-based method a little stronger. In Fig. 5.11b and 5.11c, a degradation of performance for both methods is witnessed, with the coherent method still performing better than the

incoherent energy-based method. In Fig. 5.11d, the incoherent method fails, whereas small peaks at the resonant frequencies are still seen using the coherent method.

The main conclusion drawn from Fig. 5.10 and 5.11 is the better, more peaked performance of the coherent method,  $\hat{\mathbf{q}}(\omega)$ , over the incoherent method,  $\hat{\mathbf{e}}(\omega)$ . These results can be distilled into a classification metric by calculating the sample variance or sample kurtosis of the above vectors and comparing these values at various signal-to-noise ratios to the variance or kurtosis of the same processing performed on a bubble.

Figure 5.12 shows the result of just such a processing. Although the sample variance the coherent processing (black in Fig. 5.12a) is, in general, higher than that of the incoherent processing (gray in Fig. 5.12a) the separation of the coherent method when applied to the shell (solid line) and the bubble (dashed line) is greater than the separation of the incoherent method applied to the shell and the bubble. The coherent method recognizes a difference between the two down to an SNR of -10 dB, whereas the incoherent method fails at this reverb level. This result was previously seen in Fig. 5.11d. Since the coherent PCA-based method yields a more peaked result, the sample kurtosis of  $\hat{\mathbf{e}}(\omega)$  and  $\hat{\mathbf{q}}(\omega)$ , shown in Fig. 5.12b, yields another classification metric. In this case, the coherent method recognizes a difference between the shell and the bubble at SNRs as low as -20 dB, whereas this metric is rather poor for the incoherent method, failing at an SNR of -5 dB.

## 5.4 Experimental Proposal

Although both forms of processing perform well when a vertical array is used at high signal-to-noise levels, such a configuration would be impractical to realize at-sea for real-world application. Of great interest would be the results of this processing performed on a dataset realized from a horizontal array towed from an AUV.

The strength of the processing, in both the incoherent and coherent case, is based on “averaging” away the frequency-domain peaks caused by waveguide interference, leaving only those peaks emitted from a resonant target. Therefore, such a towed source would have to sample the wavenumber space efficiently, which is done much more easily with a vertical array than a horizontal one [7]. The best solution to this would seem to be a broadside array as close as feasible to the target. The point of acoustic detection and classification of a target in MCM, of course, is to not be close to the target, so a compromise in distance must be made.

## 5.5 Conclusion

This paper has introduced and compared two forms of processing to classify a target as either resonant or non-resonant by using the back-scattered field from that target. The two processing methods are an incoherent, energy-based method, and a coherent PCA-based method. Comparison of the two methods in simulation shows the benefit of the coherent method over the incoherent method in detecting resonances in the presence of noise. Lastly, an experiment to test the practicality of the processing for real-world MCM is proposed.



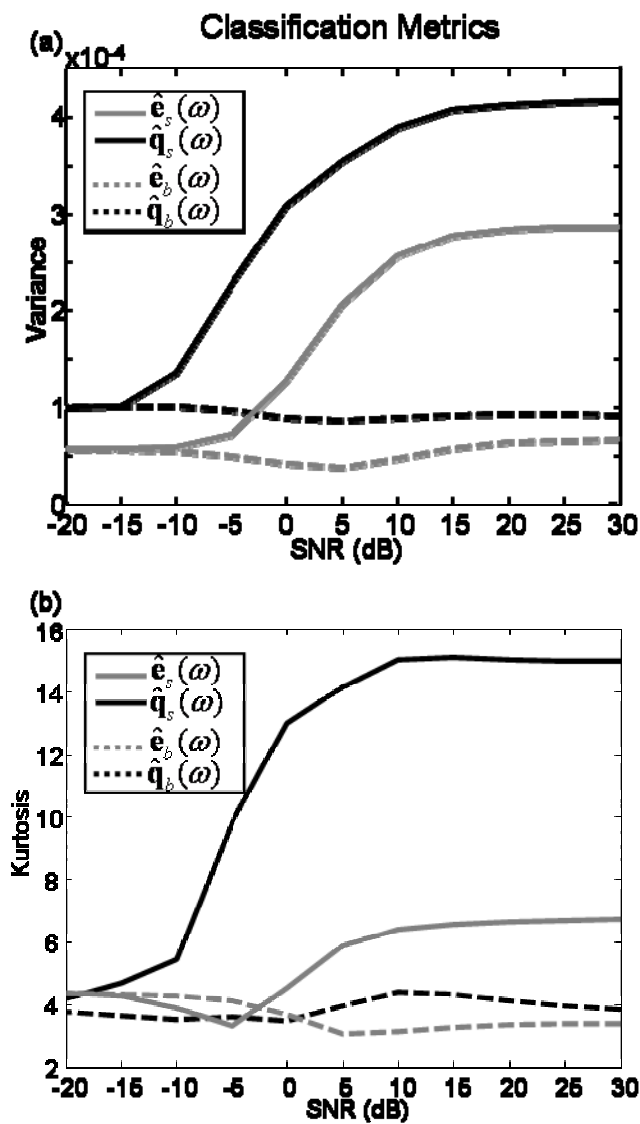


Figure 5.12: a) Sample variance of the frequency vectors corresponding to the incoherent processing (gray) and coherent processing (black). The solid lines correspond to the processing performed on the flush-buried shell, and the dashed lines correspond to the processing performed on the bubble for comparison. The coherent processing outperforms the incoherent processing by approximately 5 dB, using this metric. b) The sample kurtosis, which is high for peaky vectors, of the frequency vectors corresponding to the incoherent processing (gray) and coherent processing (black). The solid lines correspond to the processing performed on the flush-buried shell, and the dashed lines correspond to the processing performed on the bubble for comparison. Using this metric, classification using the coherent PCA-based method is possible as low as -20 dB.

## REFERENCES

1. A. Tesei, A. Maguer, W.L.J. Fox, R. Lim, and H. Schmidt, "Measurements and modeling of acoustic scattering from partially and completely buried spherical shells," *J. Acous. Soc. Am.*, vol. 112, pp. 1817-1830, 2002.
2. A. Tesei, W.L.J. Fox, A. Maguer, and A. Løvik, "Target parameter estimation using resonance scattering analysis applied to air-filled, cylindrical shells in water," *J. Acous. Soc. Am.*, vol. 108, pp. 2891-2900, 2000.
3. A. Maguer, W.L.J. Fox, H. Schmidt, E. Pouliquen, and E. Bovio, "Mechanisms for subcritical penetration into a sandy bottom: Experimental and modeling results," *J. Acous. Soc. Am.*, vol. 107, 1215-1225, 2000.
4. H. Schmidt and J. Lee, "Physics of 3-d scattering from rippled seabeds and buried targets in shallow water," *J. Acous. Soc. Am.*, vol. 105, 1605-1617, 1999.
5. C. Prada, S. Manneville, D. Spoliansky, and M. Fink, "Decomposition of the time reversal operator: Detection and selective focusing on two targets," *J. Acous. Soc. Am.*, vol. 99, pp. 2067-2076, 1996.
6. T.K. Moon and W.C. Stirling, *Mathematical Methods and Algorithms for Signal Processing*, Prentice Hall, 2000.
7. M.R. Dungan and D.R. Dowling, "Orientation effects on linear time reversing array retrofocusing in shallow water," *J. Acous. Soc. Amer.*, vol. 112, pp. 1842-1852, 2002."